

Fast initialization of a high-fidelity quantum register using optical superlattices.

B. Vaucher, S.R. Clark, U. Dörner, and D. Jaksch

Clarendon Laboratory, University of Oxford, Parks Road, OX1 3PU, United Kingdom

E-mail: benoit.vaucher@merton.ox.ac.uk

PACS numbers: 03.75.Lm, 03.75.-b

Submitted to: *New J. Phys.*

Abstract. We propose a method for the fast generation of a quantum register of addressable qubits consisting of ultracold atoms stored in an optical lattice. Starting with a half filled lattice we remove every second lattice barrier by adiabatically switching on a superlattice potential which leads to a long wavelength lattice in the Mott insulator state with unit filling. The larger periodicity of the resulting lattice could make individual addressing of the atoms via an external laser feasible. We develop a Bose-Hubbard-like model for describing the dynamics of cold atoms in a lattice when doubling the lattice periodicity via the addition of a superlattice potential. The dynamics of the transition from a half filled to a commensurately filled lattice is analyzed numerically with the help of the Time Evolving Block Decimation algorithm and analytically using the Kibble-Zurek theory. We show that the time scale for the whole process, i.e. creating the half filled lattice and subsequent doubling of the lattice periodicity, is significantly faster than adiabatic direct quantum freezing of a superfluid into a Mott insulator for large lattice periods. Our method therefore provides a high fidelity quantum register of addressable qubits on a fast time scale.

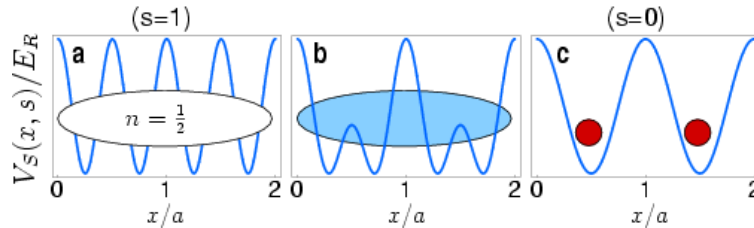


Figure 1. (a) The initial profile of the lattice is associated with the value of $s = 1$. The periodicity of the lattice is then progressively doubled (b) until it reaches its final profile (c) associated with the parameter $s = 0$. The number of sites M corresponds to the number of unit cells in the large lattice limit. By starting with a filling factor of $n = 1/2$, this procedure leads to a lattice with filling factor of $n = 1$.

1. Introduction

Systems of cold atoms trapped in optical lattices provide the unique opportunity to coherently manipulate a large number of atoms [1, 2, 3]. The remarkable degree of experimental control offered by these systems, as well as the possibility to use the internal hyperfine states of the atoms to encode qubits, make them particularly suited for quantum information processing (QIP). In this context, optical lattices in a Mott-insulating (MI) state with unit filling can be viewed as the realization of a quantum register, and it is possible to collectively manipulate the qubits stored in such a register experimentally [4, 5]. However, in many quantum computing schemes based on neutral atoms stored in optical lattices the application of single qubit gates [3] or single qubit measurements [6] requires the ability to address single atoms with a focused laser beam. This remains experimentally challenging since these operations have to be performed without perturbing the state of other atoms in their vicinity.

A number of strategies have been proposed to circumvent this problem by using global operations [7, 8, 9], e.g. via “marker atoms” which are moved to a particular lattice site and interact with the corresponding register qubit such that an external laser affects only that qubit [10]. Another way is simply to use a quantum register in which the atoms are distant enough such that they can be addressed individually by a laser. This method requires an optical lattice with filling factor $n = 1$ in the MI state with a sufficiently large distance between the atoms [11]. The initialization time of a MI state is proportional to the tunneling time of the atoms between neighboring sites. Therefore, by using the conventional method of quantum-freezing a superfluid (SF) state [4, 12, 13, 14], it scales exponentially with the lattice spacing [15, 16, 17].

In this paper we propose an alternative method to generate a long wavelength lattice with one atom per site in the MI state. Starting with a one dimensional lattice with a short period—and hence a short initialization time—and filling factor $n = 1/2$ we remove every second potential barrier by adiabatically turning on a superlattice. This superlattice potential has already been experimentally realized [18, 19]. This procedure eventually leads to a long wavelength lattice in which the periodicity has been doubled and where the atoms are in a MI state with $n = 1$ (see figure 1). This scheme does not require changing the angles of the intersecting laser beams. Furthermore, we show that our method allows for the initialization of a MI state with unit filling factor on a time-scale which, although scaling exponentially with the

final lattice spacing, is approximately one order of magnitude smaller than the direct quantum-freezing method. Although we only consider the case of an homogeneous lattice, the results presented in this paper extend to the case of weak harmonic confinements, quartic [20] and box traps [21].

This paper is structured as follows: In Sec. 2 we introduce the model used to describe the system dynamics. In Sec. 3.1 we discuss ground state properties, particularly two-site correlation functions and quasi momentum distributions. Also, we present and discuss numerical results for the probability of staying in the ground state during the transition depending on the speed of the ramping. In Sec. 3.2 we apply the analytical Kibble-Zurek theory and compare it with our numerical results. Finally, we summarize and conclude in Sec. 4.

2. Model

We consider a gas of interacting ultracold bosonic atoms loaded into a three dimensional optical lattice. The lattice is formed by pairwise orthogonal standing wave laser fields and its optical potential is given by [22]

$$V_{OL}(\mathbf{r}, s) = V_S(x, s) + V_T [\sin^2(kz) + \sin^2(ky)]. \quad (1)$$

Here V_T is the depth of the potential in the y - and z -directions created by pairs of lasers with wave number $k = 2\pi/\lambda$, wave length λ and period $a_T = \lambda/2$. The extension to the case of different optical potentials in the y - and z -directions is straightforward. In the x -direction two pairs of laser beams with a long wavelength λ_L and short wavelength $\lambda_S = \lambda_L/2$ are applied. The potential in the x -direction is thus given by

$$V_S(x, s) = V_0 (1 - s) \sin^2(k_L x) + V_0 s \sin^2(k_S x), \quad (2)$$

with V_0 the depth of the lattice, $k_L = 2\pi/\lambda_L$ and $k_S = 2\pi/\lambda_S$. The depths of the potentials will be expressed in units of the recoil energy $E_R = k_L^2/2m$ with m the mass of the atoms (taking $\hbar = 1$ throughout). The parameter $s \in [0, 1]$ is determined by the relative intensities of the two pairs of lasers. By changing s from 1 to 0 the lattice profile is continuously transformed from a sinusoidal potential with a small period $a_S = \lambda_S/2$ to one with a long period $a = \lambda_L/2$, thus halving the number of lattice sites per unit length along the x -direction (see figure 1). The lattice constant a corresponds to the size of a unit cell for $s < 1$ ‡. We refer to the lattice profile with parameters $s = 1$ and $s = 0$ as to the *small lattice limit* and the *large lattice limit*, respectively.

The Hamiltonian of the system in second quantization reads

$$\hat{H} = \int d\mathbf{r} \hat{\psi}^\dagger(\mathbf{r}) \hat{h}_0(\bar{\mathbf{r}}) \hat{\psi}(\mathbf{r}) + \frac{g}{2} \int d\mathbf{r} \hat{\psi}^\dagger(\mathbf{r}) \hat{\psi}^\dagger(\mathbf{r}) \hat{\psi}(\mathbf{r}) \hat{\psi}(\mathbf{r}), \quad (3)$$

where $\hat{h}_0(\bar{\mathbf{r}}) = -(1/2m)\nabla^2 + V_{OL}(\bar{\mathbf{r}})$ is the one-particle Hamiltonian. The symbol $\bar{\mathbf{r}} = (\mathbf{r}, s)$ represents the position variable \mathbf{r} and lattice parameter s . The interaction between the atoms is modelled by s -wave scattering with $g = 4\pi a_s/m$ where a_s is the s -wave scattering length. The bosonic field operators obey the usual commutation relations $[\psi(\mathbf{r}), \psi^\dagger(\mathbf{r}')] = \delta(\mathbf{r} - \mathbf{r}')$ with δ denoting the Dirac delta function.

We restrict our considerations to the case where V_T is sufficiently large so that motion along the y - and z -directions is frozen. The dynamics of the system is then effectively one dimensional along the x -direction. As shown in figure 2a the two lowest

‡ To avoid any discontinuity, we work with a lattice periodicity of a even in the case $s = 1$.

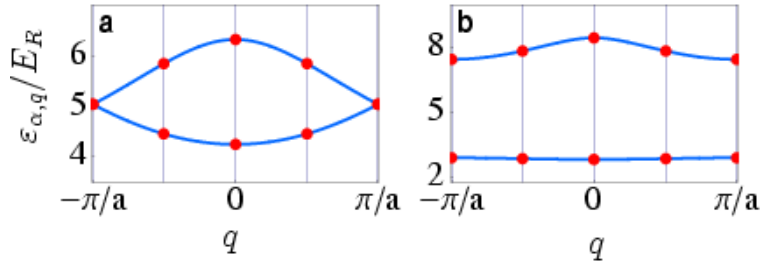


Figure 2. Band structure along the x -direction in (a) the small and (b) large lattice limit for $V_0 = 10E_R$. The points represent the values of q for $q = 0, \pi/a, \pi/2a$. The value of $\varepsilon_{\alpha,q}$ corresponds to the energy of single-particles with momentum q in the α -th Bloch band. In the small lattice limit, the two first Bloch bands are connected.

bands of the Hamiltonian $\hat{h}_{0,x} = -(1/2m)(d/dx)^2 + V_S(x, s)$ are separated in energy by much less than the typical motional excitation energy $E_{\text{ex}} = \sqrt{4V_0E_R}$ [22] for values $s \approx 1$ §. Therefore, despite assuming that atoms loaded into the lattice are ultracold, we have to consider the two lowest Bloch bands in x -direction to obtain an accurate description of the atomic dynamics. However, excitations to higher bands in the y - and z -directions are neglected in our investigations since we assume that the temperature of the atomic cloud is $k_B T \ll E_{\text{ex}}$. We then expand the bosonic field operator as

$$\hat{\psi}(\bar{\mathbf{r}}) = \sum_{i=1}^M \phi_{a,i}(\bar{\mathbf{r}}) \hat{a}_i + \sum_{i=1}^M \phi_{b,i}(\bar{\mathbf{r}}) \hat{b}_i, \quad (4)$$

where M is the number of lattice sites and $\hat{\alpha}_i^\dagger$ ($\alpha = a, b$) creates a particle in the mode associated with the localized function $\phi_{\alpha,i}(\bar{\mathbf{r}})$ centered at site i . The mode functions $\phi_{\alpha,i}(\bar{\mathbf{r}}) = w_{\alpha,i}(x, s)W_{i,0}(y)W_{i,0}(z)$ are factorized into a product of well localized Wannier functions (WF) $W_{i,0}$ of the lowest Bloch band in the y - and z -directions [23] and mode functions $w_{\alpha,i}(x, s)$ in x -direction.

The aim of the next section is to describe the single particle dynamics in the tight binding (TB) approximation. If we were to use Wannier functions for $w_{\alpha,i}(x, s)$ this approximation would restrict our model to sinusoidal Bloch bands [24]. Because of the deviation of the lowest two bands from a sinusoidal dispersion relation (see figure 2a) when $s \approx 1$ we instead use generalized Wannier function (GWFs) for $w_{\alpha,i}(x, s)$ (see Appendix A for a detailed definition and a description of their properties) [25]. By exploiting the optimization procedure described in Appendix A we calculate GWFs $w_{\alpha,i}(x, s)$ which are well localized at lattice sites i . Typical shapes of GWFs and the effects of optimizing their localization are shown in figure 3. We note that these GWFs are in general composed of superpositions of Bloch orbitals of both bands and are not related to Wannier functions by a local transformation. Only when $s \approx 0$ the $w_{\alpha,i}(x, s)$ are equivalent to the Wannier functions of the first and the second Bloch band, respectively. Finally, they are always (anti-)symmetric with respect to the center of the lattice site i for $\alpha = a$ ($\alpha = b$).

§ The two lowest bands form two segments of the lowest Bloch band if a cell size of $a/2$ is used in the case $s = 1$.

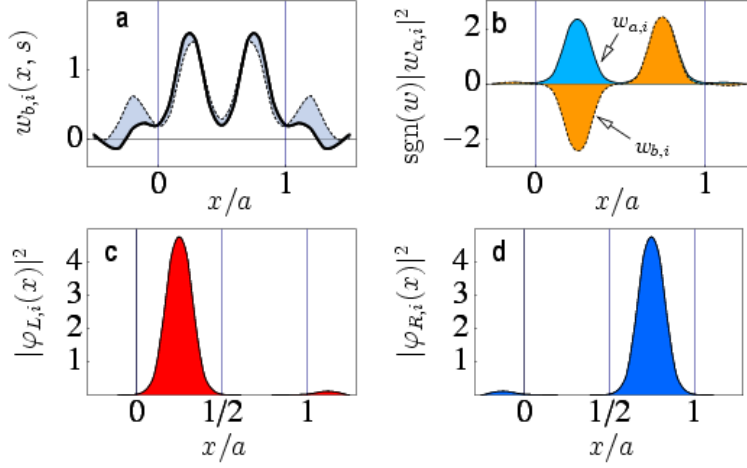


Figure 3. (a) Optimized (thick line) and non-optimized (dashed line) GWFs associated with the first mode for $V_0 = 30E_R$ and the lattice profiles $s = 1$. The area between the optimized and non-optimized mode functions is shaded in order to illustrate how the localization procedure reduces the spread of the optimized function. (b) The square of the mode functions for $V_0 = 30E_R$ and $s = 1$. By combining the mode functions shown in (b), we can construct two new mode functions corresponding to particles localized in either the left (c) or the right (d) well of a given site.

2.1. Single-particle Hamiltonian

Inserting the approximate field operator equation (4) into the first term of equation (3) yields the single-particle part of the Hamiltonian in terms of \hat{a}_i^\dagger and \hat{b}_i^\dagger . Applying the tight binding approximation, which amounts to keeping only nearest-neighbor hopping terms, the single-particle Hamiltonian can be approximated by

$$\begin{aligned}
 \hat{H}_0(s) = & \sum_{i=1}^{M-1} \left(J_{bb}(s) \hat{b}_i^\dagger \hat{b}_{i+1} - J_{aa}(s) \hat{a}_i^\dagger \hat{a}_{i+1} + \text{h.c.} \right) \\
 & + \sum_{i=1}^{M-1} \left(J_{ba}(s) \hat{b}_i^\dagger \hat{a}_{i+1} - J_{ab}(s) \hat{a}_i^\dagger \hat{b}_{i+1} + \text{h.c.} \right) \\
 & + \sum_{i=1}^M \left(V_a(s) \hat{a}_i^\dagger \hat{a}_i + V_b(s) \hat{b}_i^\dagger \hat{b}_i \right), \tag{5}
 \end{aligned}$$

where

$$J_{\alpha\beta}(s) = \int dx w_{\alpha,i}^*(x,s) \hat{h}_{0,x}(s) w_{\beta,i+1}(x,s), \tag{6}$$

is the hopping matrix element between neighboring sites along the x -axis and

$$V_\alpha(s) = \int dx w_{\alpha,i}^*(x,s) \hat{h}_{0,x}(s) w_{\alpha,i}(x,s), \tag{7}$$

is the local on-site energy of a particle in mode α . Note that hopping between modes a and b within one site is not allowed by the symmetry properties of the GWFs.

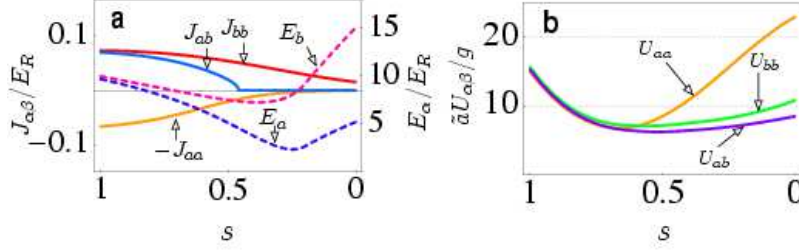


Figure 4. Parameters of the effective Hamiltonian \hat{H}_{eff} as functions of s for a lattice depth of $V_0 = 30E_R$ and $V_T = 60E_R$ with $\tilde{a} = a a_T^2$. The hopping matrix elements (a) have been calculated using the method described in Appendix B, while the on-site interaction energies (b) are calculated using optimized GWFs.

However, the inclusion of non-zero hopping matrix elements J_{ab} and J_{ba} is essential to accurately reproduce the single particle behaviour of the full Hamiltonian (3). The symmetry properties of WFs would not allow the inclusion of these terms [24].

For periodic boundary conditions, the parameters V_α and $J_{\alpha,\beta}$ can be found from the band structure without explicit calculation of the mode functions (see Appendix B). The numerical values of V_α and $J_{\alpha,\beta}$ for $V_0 = 30E_R$ are shown in figure 4a. Using these parameters, we find that $\hat{H}_0(s)$ very accurately reproduces the band structure of the exact Hamiltonian for all values of s , thus justifying the utilization of the TB approximation and the corresponding GWFs.

2.2. Interaction Hamiltonian

To calculate the interaction matrix elements of \hat{H} the explicit form of the localized GWFs is needed. We find that for $V_0 > 10E_R$, off-site interaction terms are at least two orders of magnitude smaller than on-site interactions. We therefore only keep the dominant on-site terms and find the interaction Hamiltonian \hat{H}_I

$$\begin{aligned} \hat{H}_I(s) = & \sum_{i=1}^M \frac{U_{aa}(s)}{2} \hat{n}_i^a (\hat{n}_i^a - 1) + \frac{U_{bb}(s)}{2} \hat{n}_i^b (\hat{n}_i^b - 1) \\ & + \sum_{i=1}^M \frac{U_{ab}(s)}{2} \left(4\hat{n}_i^a \hat{n}_i^b + \hat{b}_i^\dagger \hat{b}_i^\dagger \hat{a}_i \hat{a}_i + \hat{a}_i^\dagger \hat{a}_i^\dagger \hat{b}_i \hat{b}_i \right), \end{aligned} \quad (8)$$

where $\hat{n}_i^a = \hat{a}_i^\dagger \hat{a}_i$ and $\hat{n}_i^b = \hat{b}_i^\dagger \hat{b}_i$ are the site-occupation number operators. The on-site interaction matrix elements are given by

$$U_{\alpha,\beta}(s) = g \int d\mathbf{r} w_{\alpha,i}^*(\mathbf{r}) w_{\beta,i}^*(\mathbf{r}) w_{\alpha,i}(\mathbf{r}) w_{\beta,i}(\mathbf{r}). \quad (9)$$

The numerical values of $U_{\alpha,\beta}$ as a function of the lattice profile s are shown in figure 4b. Figure 4b shows that their values become equal as $s \rightarrow 1$ for sufficiently large V_0 .

Combining the single- and two-particle contributions the effective Hamiltonian describing the system dynamics is given by

$$\hat{H}_{\text{eff}}(s) = \hat{H}_0(s) + \hat{H}_I(s). \quad (10)$$

By using $\hat{H}_{\text{eff}}(s)$ for s varying in time we implicitly assume that the system adiabatically follows changes in the mode functions $w_{\alpha,i}$. For all dynamical

calculations carried out in this work we have carefully chosen the time dependence of s so that such non-adiabatic contributions can safely be neglected.

2.3. Limiting cases

In the small lattice limit ($s = 1$), the superpositions $\varphi_{L,i} = (w_{a,i} - w_{b,i})/\sqrt{2}$ and $\varphi_{R,i} = (w_{a,i} + w_{b,i})/\sqrt{2}$ correspond to mode functions localized in the left and in the right well of site i respectively (see figure 3c and 3d). The associated bosonic operators are defined by

$$\hat{c}_{L,i}^\dagger = \frac{1}{\sqrt{2}}(\hat{a}_i^\dagger - \hat{b}_i^\dagger), \quad \hat{c}_{R,i}^\dagger = \frac{1}{\sqrt{2}}(\hat{a}_i^\dagger + \hat{b}_i^\dagger). \quad (11)$$

Given that the new mode functions are sufficiently localized within each well, the parameters of \hat{H}_{eff} for $s = 1$ can be written as

$$V_a = E - J, \quad V_b = E + J, \quad J_{\alpha,\beta} = J/2, \quad U_{\alpha,\beta} = U/2, \quad (12)$$

where $J = \int dx \varphi_{R,i}^* \hat{h}_{0,x} \varphi_{L,i+1}$, $E = \int dx \varphi_{L,i}^* \hat{h}_{0,x} \varphi_{L,i}$ and $U = g \int dx |\varphi_{R,i}|^4$. Notice that the parameters shown in figure 4 are consistent with these equations. Expressing the Hamiltonian (10) in terms of the operators $\hat{c}_{\alpha,i}^\dagger$ ($\alpha = L, R$) and using the parameters 12 we find that

$$H'_{\text{eff}} = -J \sum_{i'=1}^{2M-1} \hat{c}_{i'}^\dagger \hat{c}_{i'+1} + \text{h.c.} + E \sum_{i'=1}^{2M} \hat{c}_{i'}^\dagger \hat{c}_{i'} + \frac{U}{2} \sum_{i'=1}^{2M} \hat{c}_{i'}^\dagger \hat{c}_{i'}^\dagger \hat{c}_{i'} \hat{c}_{i'}, \quad (13)$$

where

$$\hat{c}_{i'}^\dagger = \begin{cases} \hat{c}_{L, i'/2}^\dagger & \text{if } i' \text{ odd,} \\ \hat{c}_{R, i'/2}^\dagger & \text{if } i' \text{ even.} \end{cases} \quad (14)$$

Therefore, as expected, $\hat{H}_{\text{eff}}(s = 1)$ is equivalent to the one-band Bose-Hubbard model (BHM) [22] with $2M$ sites.

The mode functions keep their symmetry with the two peaks moving towards the center of the cell when s is decreased. When $s \approx 0$ is reached $w_{a,i}(x, s)$ and $w_{b,i}(x, s)$ are equivalent to the Wannier functions of the first and the second Bloch band, respectively. In this limit we obtain a standard two band Bose-Hubbard model for M sites.

3. Time-scale for the preparation of the quantum register

In this section we present numerical as well as analytical results characterizing the ground state properties of the system and the time-scale necessary to initialize the quantum register.

3.1. Numerical results

The numerical calculations have been carried out using both the exact matrix representation of the Hamiltonian \hat{H}_{eff} and the Time-Evolving Block Decimation (TEBD) algorithm (see Appendix C for details).

We have evaluated the ground state and dynamical properties of our system for two different values of g corresponding to different interaction regimes. These values have been chosen such that in the large lattice limit (with filling factor $n = 1$) the

ground state is a Mott-insulator state for g_1 and g_2 with $J_{aa}/U_{aa} < 0.3$ [26]. In the small lattice limit, g_1 and g_2 produce ground states corresponding to a strongly interacting Tonks-Girardeau (TG) gas ($U/J = 215$) and a superfluid ($U/J = 7$), respectively.

3.1.1. Ground states properties In the large lattice limit, the ground state $|\psi_{0,L}\rangle$ of the system is populated exclusively by particles in the lowest Bloch band, i.e. a -mode particles. Therefore, in this limit, we only consider the one-particle density matrix given by

$$\rho_{ij}^L(\psi) = \langle \psi | \hat{a}_i^\dagger \hat{a}_j | \psi \rangle, \quad (15)$$

where $|\psi\rangle$ is the state of the system. The quasi-momentum distribution of particles in the a -mode is given by [27]

$$n_q^L(\psi) = \frac{1}{M} \sum_{i,j=1}^M e^{-iqa(i-j)} \rho_{ij}^L(\psi). \quad (16)$$

As expected, in this limit and for commensurate filling $n = 1$ the ground state is a Mott-insulator for both values of g (see figures 5a–d). The quasi-momentum distributions show that in this limit particles are uniformly distributed in the first band (see figures 5a and 5c).

In the small lattice limit, the one-particle density matrix is given by

$$\rho_{i'j'}^S(\psi) = \langle \psi | \hat{c}_i^\dagger \hat{c}_{j'} | \psi \rangle, \quad (17)$$

where the operators \hat{c}_i^\dagger are constructed from the \hat{a}_i^\dagger and \hat{b}_i^\dagger operators using the transformations (11). The quasi-momentum distribution is given by

$$n_q^S(\psi) = \frac{1}{2M} \sum_{i',j'=1}^{2M} e^{-iq\frac{a}{2}(i'-j')} \rho_{i'j'}^S(\psi). \quad (18)$$

In this limit (with filling factor $n = 1/2$), the characteristics of the ground state $|\psi_{0,S}\rangle$ depend on the value of g . For $g = g_1$, the ratio $U/J = 215$ and the ground state's correlations as well as the quasi-momentum distributions (see figures 5e–f) are characteristic of a TG gas (see e.g. [28] and references therein). The value $g = g_2$ yields the ratio $U/J = 7$ and the system exhibits the behaviour of a superfluid (see figures 5g–h), with particles occupying mainly the $q = 0$ momentum state. Notice that one-dimensional systems described by the BHM with a fixed filling factor $n = 1$ cross the MI-SF phase boundary at the critical point $(J/U)_c \approx 0.3$ [26]. Thus, in our case the superfluid behavior of the system in the small lattice limit is due to the fractional filling of the lattice.

3.1.2. Simulation of the dynamics Starting from a system with half-filling and a lattice profile $s = 1$, we investigate the time-scale required to obtain a nearly perfect MI state—or quantum register—with filling factor $n = 1$ by ramping the lattice profile down to $s = 0$. The quality of the register is determined by the fidelity

$$F = |\langle \psi | \psi_{0,L} \rangle|^2, \quad (19)$$

defined as the overlap between the state of the system $|\psi\rangle$ at the end of the ramping process and the ground state in the large lattice limit $|\psi_{0,L}\rangle$. Furthermore, we calculate the fluctuations of the number of particles in the a -mode at site i

$$\Delta n_{a,i} = \sqrt{\langle (\hat{n}_i^a)^2 \rangle - \langle \hat{n}_i^a \rangle^2}, \quad (20)$$

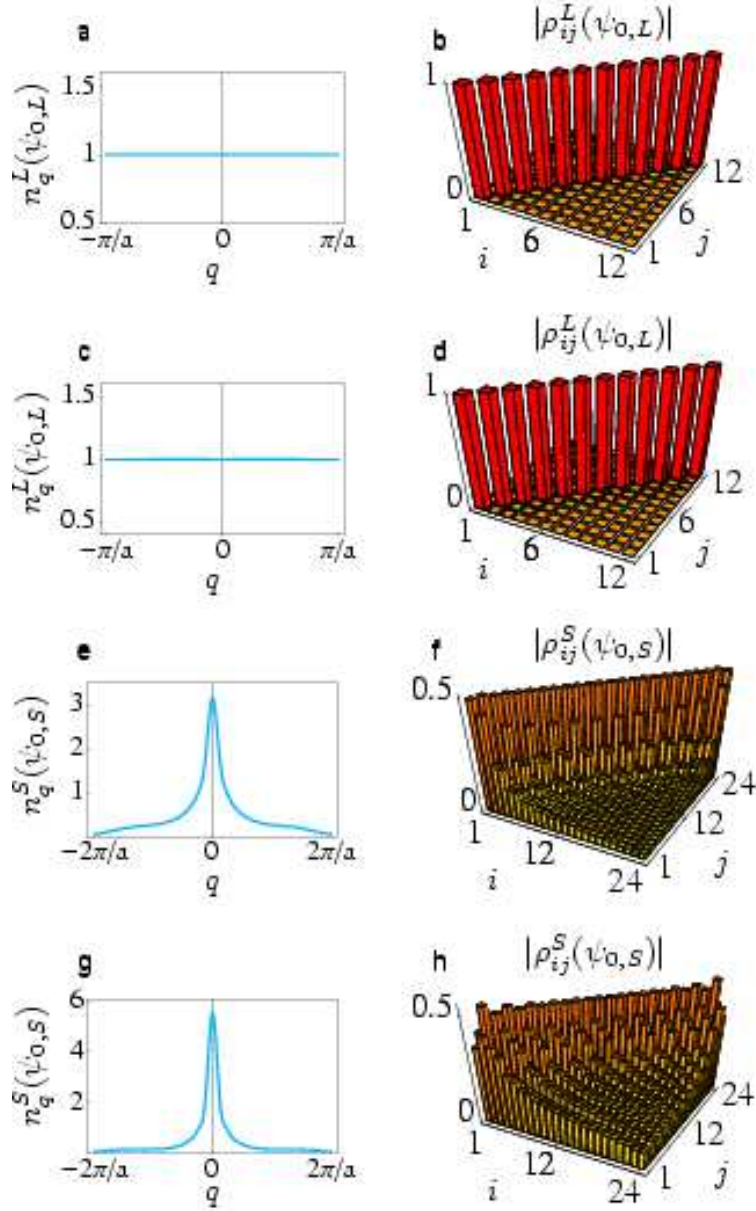


Figure 5. Ground state one-particle density matrix and quasi-momentum distribution for $M = 12$ lattice sites and the parameters of figure 4. The figures (a-d) correspond to the large lattice limit and the figures (e-h) to the small lattice limit. The quasi-momentum distribution (a), (e) and one-particle density matrix (b), (f) are for $g = g_1$. The quasi-momentum distribution (c), (g) and one-particle density matrix (d), (h) are for $g = g_2$.

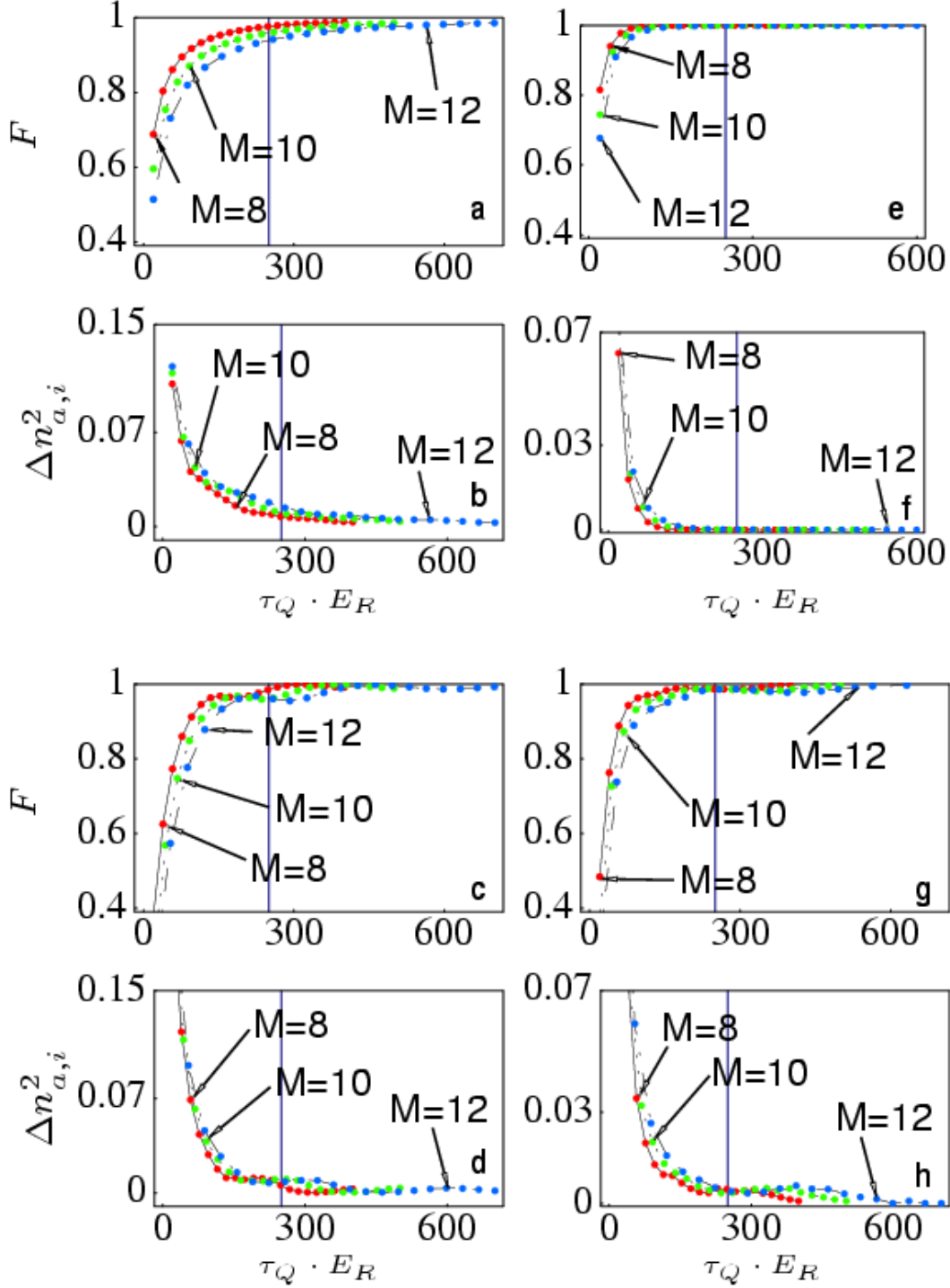


Figure 6. Dynamical simulation of \hat{H}_{eff} using the parameters shown in figure 4 for two different values of g . The ramping strategies s_{gap} and s_{man} are shown in figure 7a. Simulation results for the fidelity and particle-number fluctuations using: (a–b) a linear ramp and $g = g_1$; (c–d) a linear ramp and $g = g_2$; (e–f) the ramp s_{gap} and $g = g_1$; (g–h) the ramp s_{man} and $g = g_2$. The vertical lines indicate the value of the particle tunneling time ($t_{\text{tun}} \sim 1/J_{aa}$) in the large lattice limit.

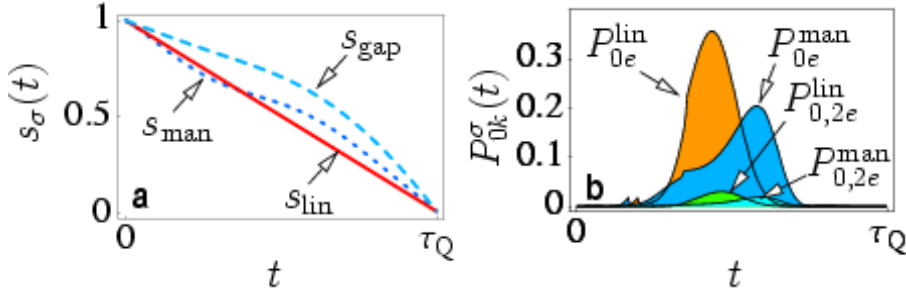


Figure 7. (a) Different ramps used in our numerical calculations. (b) Transition probability between the ground and the first (labeled by e) and second (labeled by $2e$) excited states as a function of time for the ramps s_{lin} and s_{man} . The transition probabilities have been calculated via the exact diagonalization of \hat{H}_{eff} for $M = 4$ and a quench time of $\tau_Q = 20/E_R$.

where $\langle \circ \rangle = \langle \psi | \circ | \psi \rangle$. Since particle-number fluctuations are suppressed in a MI state, non-zero fluctuations indicate the presence of excitations, such as double occupancies or particles in the second band, in the final state.

We test different ramps by simulating the system dynamics between $t_i = 0$ to $t_f = \tau_Q$ where τ_Q is the ramping time (the time required to complete the ramping process from $s = 1$ to $s = 0$). Here, each ramp σ corresponds to a function $s = s_\sigma(t)$ varying from $s_\sigma(0) = 1$ to $s_\sigma(\tau_Q) = 0$.

For linear ramping we use $s_{\text{lin}}(t) = (\tau_Q - t/E_R)/\tau_Q$. The fidelity and particle-number fluctuations obtained using this strategy for different quench times and $g = g_1$ and $g = g_2$ are shown in figures 6a–d. The linear ramp is shown in figure 7a.

Another ramping strategy we use consists of adapting the velocity of the ramp proportionally to the energy gap between the ground and the first excited state. This ramp is denoted by $s_{\text{gap}}(t)$. We evaluate the ramp function $s_{\text{gap}}(t)$ numerically (see Appendix D) for a system with $M = 4$ sites and $V_0 = 30E_R$. The ramp $s_{\text{gap}}(t)$ for $g = g_1$ is shown in figure 7a. We expect this ramping strategy to be more efficient than the linear one, since accelerating the ramp when the gap is large while slowing it down when the gap is small should suppress transitions of particles to excited levels. Our numerical calculations have shown that when $g = g_1$, the utilization of this ramp does indeed reduce the quench time needed to obtain a nearly perfect fidelity to a half of the tunneling time in the large lattice limit (see figure 6e–f). For $g = g_2$, we find that compared to $s_{\text{lin}}(t)$, this strategy only marginally improves the fidelity.

In order to reduce the time required to obtain a given fidelity for $g = g_2$, a more sophisticated ramping strategy is needed. In the following, we provide a simple method to estimate the efficiency of different ramps without running a complete dynamical simulation of the system. The transition probability between the ground and some excited state $|k\rangle$ at time t for a ramp σ is approximately given by [29]

$$P_{0k}^\sigma(t) \approx \frac{2}{\omega_{0k}^2} \left| \langle 0 | \frac{d}{dt} | k \rangle \right|^2 [1 - \cos(\omega_{0k}t)], \quad (21)$$

where $|k\rangle = |k(\sigma, t)\rangle$ is the k -th instantaneous eigenstate^{||} of $\hat{H}_{\text{eff}}(s_\sigma(t))$ and ω_{0k} is the transition frequency between the ground state and $|k\rangle$. Therefore, the assessment of the efficiency of a ramp can be done by evaluating the functional

$$A(\sigma, \tau_Q) = \frac{1}{\tau_Q} \sum_k \int_0^{\tau_Q} dt P_{0k}^\sigma(t), \quad (22)$$

where the index k runs over all the values associated with levels connected to the ground state. The functional $A(\sigma, \tau_Q)$ corresponds to the average transition probability per unit time for a given strategy σ and quench time τ_Q . We calculate the value of the functional $A(\sigma, \tau_Q)$ numerically via exact diagonalization of \hat{H}_{eff} for a small system. This method allows to optimize ramps by minimizing the value of $A(\sigma, \tau_Q)$. The optimized ramp for a small system is then used in the simulation of larger systems. For instance, the strategy $s_{\text{man}}(t)$ shown in figure 7a was designed and optimized manually using this method. For $g = g_2$, we find that $A(\text{lin}, \tau_Q)/A(\text{man}, \tau_Q) \approx 2.3$ for $\tau_Q = 20/E_R$ (see figure 7b), thus showing the better efficiency of the strategy $s_{\text{man}}(t)$ compared to $s_{\text{lin}}(t)$. As shown in figure 6, dynamical simulations of the system with $g = g_2$ confirm that this strategy reduces the time required to obtain a given fidelity.

For systems initially in the superfluid regime ($g = g_2$), the fidelity curves exhibit small oscillations (see figure 6e). These can be understood from time-dependent perturbation theory as oscillations occurring when some of the frequencies involved in the Fourier decomposition of the perturbation Hamiltonian enter into resonance with system frequencies. This is expected since superfluids have a dense spectrum at low energies and are therefore likely to enter into resonance with one of the frequencies of the perturbation Hamiltonian [30]. Hence, the amplitude of the oscillations in the fidelity curve associated with a ramping strategy $s_1(t)$ should be smaller than those associated with a ramping strategy $s_2(t)$ if $A(1, \tau_Q) < A(2, \tau_Q)$ for all τ_Q . This is what is observed from our numerical simulations (see figures 6f-h).

The quasi-momentum distribution of the particles in the a -mode at the end of the different ramping processes for a system with $g = g_1$ are shown in figure 8. For the linear ramp, the quasi-momentum distribution of particles shown in figure 8a does not correspond to that of a MI state for the quench times considered. In contrast, for the ramp s_{gap} the quasi-momentum distribution becomes approximately flat for quench times of $\tau_Q > 200/E_R$. Even for the fastest ramps, we find that the occupation of the b -mode is less than 2% of the total number of particles. Thus, the experimental measure of the register fidelity can be made by comparing the quasi-momentum distribution of particles in the final state with, e.g. that shown in figure 5c.

3.1.3. Discussion of the numerical results In the BHM with $U/J \ll 1$, the tunneling time $1/J$ determines the adiabatic time-scale of the system. However, as soon as many-body interactions are sufficiently large, this time-scale often becomes very non-adiabatic [31]. The main observation that can be drawn from the numerical calculations presented in the last section is that by preparing the system in a TG state ($g = g_1$), and using an efficient ramping strategy, it is possible to initialize a very deep MI state on a time scale equivalent to half the tunneling time in the large lattice limit (see figure 6b). The time required to initialize a MI state with unit filling as well as a TG state with half filling is approximately ten times the tunneling time of

^{||} Note that neglecting non-adiabatic changes of the GWFs does not correspond to $P_{0k}^\sigma(t) = 0$ at all times.

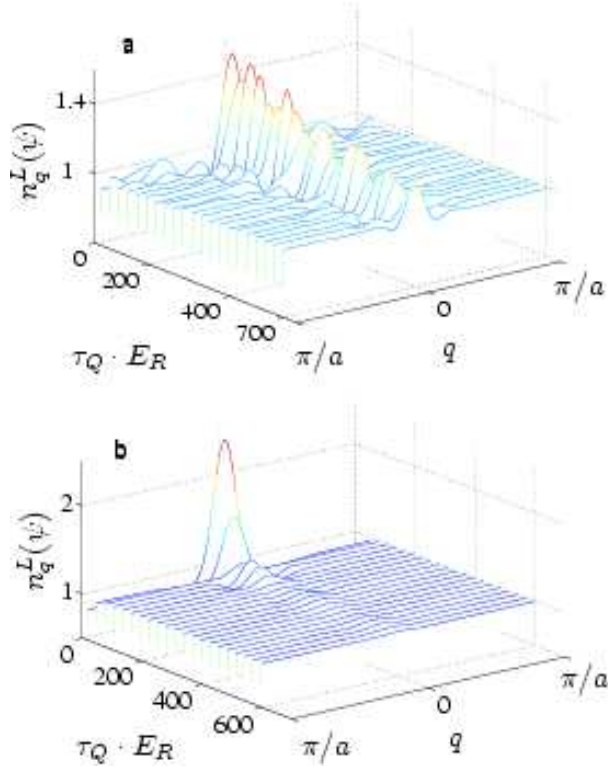


Figure 8. The quasi-momentum distributions at the end of a ramp for a system of $M = 12$ sites using the parameters shown in figure 4 for $g = g_1$. (a) s_{in} ; (b) s_{gap} .

the final system [16, 31, 32, 15]. Since the tunneling time in the large lattice limit is two orders of magnitude larger than in the small lattice limit, the total time required to initialize a MI state using our procedure is an order of magnitude faster than the direct quantum freezing method. In this estimation we assume that the initial BEC has zero temperature, i.e., we do not take the effect of defects present in the initial state into account.

The experimental realization of initial states with $g = g_1$ and $g = g_2$ can be achieved using Feshbach resonances. For a magnetic Feshbach resonance fluctuations in the magnetic field result in fluctuations of the size of the gap between the ground and the first excited state which will affect the performance of our scheme. For instance, in the case $g = g_1$ magnetic field fluctuations of 10 mG will change the gap by approximately 0.5% for ^{85}Rb or ^{133}Cs atoms [33, 34]. We assume adiabatic evolution of the system and thus these fluctuations will have negligible repercussions on the fidelity of the final state. To realize the superfluid regime with $g = g_2$ very stable magnetic fields are required. Magnetic field fluctuations of e.g. 1 mG will lead to gap fluctuations of approximately 1% in ^{23}Na and ^{85}Rb . We finally remark that our scheme could also be used without employing a Feshbach resonance. This case corresponds to an intermediate value of g between g_1 and g_2 . While a detailed analysis of the intermediate regime is beyond the scope of the present work we do not expect

qualitative differences compared to the interaction strengths considered here.

3.2. Analytical results

In this section we derive an approximate expression for the quench time required to obtain a given fidelity in the case of a linear ramp.

The energy spectrum of systems in the TG and superfluid regime is gapless ¶(see e.g. [35]), while in the Mott-insulating regime, the gap between the ground and first excited state is proportional to the on-site interaction energy [30]. Since the relaxation time $\tau(t)$ of the system—the time required by the system to adjust to a change of parameters at time t —is inversely proportional to the gap between the ground and the first excited state, the relaxation time in the small lattice limit is large, while it is small and finite in the large lattice limit. This observation suggests that the *adiabatic-impulse* (AI) assumption from Kibble-Zurek (KZ) theory can be used to evaluate the adiabaticity of a ramp with respect to the quench time [36, 37, 38].

The AI approximation is based on the following considerations: (i) When the gap between the ground and the first excited state is large, the relaxation time of the system is short and thus a system starting its evolution in the ground state remains in the ground state, i.e. its evolution is *adiabatic*. (ii) When the gap between the ground and the first excited state is small, the system’s relaxation time is large and the system no longer adapts to changes of the Hamiltonian’s parameters and its state becomes effectively frozen. The system is then in the *impulse regime*. The instant \hat{t} at which the system passes from the impulse to the adiabatic regime, and inversely, is defined by the equation [37, 36, 39]

$$\tau(\hat{t}) = \alpha \hat{t}, \quad (23)$$

where $\alpha = \mathcal{O}(1)$ is a constant. Note that \hat{t} is a time and not an operator. In the AI approximation, the time-evolution of the system is either adiabatic or impulse. Thus, the *density of defects* \mathcal{D} , which corresponds to the density of excitations caused by a change of parameters which drive the system from the impulse to the adiabatic regime can be approximated by [37]

$$\mathcal{D} \simeq |\langle \Psi_e(\hat{t}) | \Psi_g(0) \rangle|^2, \quad (24)$$

where $|\Psi_g(0)\rangle$ and $|\Psi_e(\hat{t})\rangle$ are the ground and first excited states at the initial time $t = 0$ and at time $t = \hat{t}$, respectively. Hence, without solving the time-dependent Schrödinger equation it is possible to make predictions for the density of defects (24) resulting from a given dynamical process.

In order to apply the KZ theory to our problem, we develop an effective model describing the system dynamics. A similar model was recently examined by Cucchiatti *et al.* [38]. We find from numerical calculations (see figure 7b) that most of the excitations created in the system are caused by transitions from the ground to the first excited state. Furthermore, we examined the form of the eigenvectors of the Hamiltonian (10) in both limits for different system sizes via exact diagonalization. This revealed that both the ground state and the first accessible excited state can be approximated by an expansion in only two basis states. The elements of this reduced basis set are given by

$$|1\rangle = \bigotimes_{i=1}^M |1\rangle_i, \quad (25)$$

¶ In finite size systems, the spectrum is not gapless, only very dense.

$$\begin{aligned}
|2\rangle &= (|2; 0; 1; \dots; 1\rangle + |2; 1; 0; 1; \dots; 1\rangle + |2; 1; 1; 0; 1; \dots; 1\rangle \\
&+ |1; 2; 1; 0; 1; \dots; 1\rangle + \dots) / \sqrt{M(M-1)},
\end{aligned} \tag{26}$$

where, e.g. $|2; 0; 1; \dots; 1\rangle = |2\rangle_1 \otimes |0\rangle_2 \otimes |1\rangle_3 \otimes \dots \otimes |1\rangle_M$ with $|n\rangle_i = (1/\sqrt{n!})(\hat{a}_i^\dagger)^n |\text{vac}\rangle$. The basis state $|2\rangle$ corresponds to a superposition of all possible states of a system of M particles in the a -modes with $(M-2)$ singly occupied sites, one doubly occupied site, and one empty site. In the limit $M \rightarrow \infty$, the matrix representation \hat{H}_R of Hamiltonian (10) in the reduced basis $\{|1\rangle, |2\rangle\}$ reads, up to a constant energy V_a

$$\hat{H}_R = \begin{pmatrix} 0 & \sqrt{2} J_{aa}(t) \\ \sqrt{2} J_{aa}(t) & U_{aa}(t) \end{pmatrix}. \tag{27}$$

The instantaneous eigenstates of equation (27) associated with the energies of the ground and first excited levels are given by $|g(t)\rangle = -\sin(\theta(t)/2)|1\rangle + \cos(\theta(t)/2)|2\rangle$ and $|e(t)\rangle = \cos(\theta(t)/2)|1\rangle + \sin(\theta(t)/2)|2\rangle$, respectively, with $\cos(\theta(t)) = -U_{aa}(t)/[U_{aa}(t)^2 + 8J_{aa}(t)^2]^{\frac{1}{2}}$, $\theta \in [0, \pi]$. Furthermore, we approximate the parameters J_{aa} and U_{aa} as linear functions of time

$$\begin{aligned}
J_{aa}(t) &= \Delta J_{aa}(\tau_Q - t)/\tau_Q, \\
U_{aa}(t) &= U_{\text{init}} + \Delta U_{aa}t/\tau_Q,
\end{aligned} \tag{28}$$

where $\Delta J_{aa} = |J_{aa}(s=1) - J_{aa}(s=0)|$, $\Delta U_{aa} = |U_{\text{init}} - U_{aa}(s=0)|$ and $U_{\text{init}} = \min[U_{aa}]$.

We further simplify the Hamiltonian \hat{H}_R by replacing the hopping term $J_{aa}(t)$ by its time average. Setting $J_{aa}(t) = \bar{J}_{aa}$ with $\bar{J}_{aa} = (1/\tau_Q) \int_0^{\tau_Q} dt J_{aa}(t)$ and rescaling the time as $t \rightarrow t' - (U_{\text{init}}\tau_Q/\Delta U_{aa})$ yields the transformation

$$\hat{H}_R \rightarrow \hat{H}_R = \begin{pmatrix} 0 & \sqrt{2} \bar{J}_{aa} \\ \sqrt{2} \bar{J}_{aa} & \Delta U_{aa}t'/\tau_Q \end{pmatrix}, \tag{29}$$

which turns \hat{H}_R into the Landau-Zener form $\hat{H}_R = \hat{A}t' + \hat{B}$, where \hat{A} and \hat{B} are Hermitian matrices and \hat{A} is diagonal [40, 41, 42]. The energy spectrum of the Hamiltonian (29) reproduces approximately the features of the spectrum of \hat{H}_{eff} except that the gap is overestimated in the small lattice limit.

Starting at $t = 0$ in the small lattice limit where the system is impulse, we use the AI approximation to derive the density of defects at the end of a linear ramp which drives the system to the large lattice limit, where the system is adiabatic. Defining the relaxation time as the inverse of the energy gap $1/\Delta E$ between the levels of \hat{H}_R , with $\Delta E = [(\Delta U_{aa}t'/\tau_Q)^2 + (2\sqrt{2}\bar{J}_{aa})^2]^{\frac{1}{2}}$, equation (23) can be solved analytically and the instant \hat{t} at which our system exits the impulse regime is given by

$$\hat{t} = \sqrt{\frac{\tau_Q}{\Delta U_{aa}}} \sqrt{\sqrt{\frac{1}{\alpha} + (\eta\tau_Q)^2} - \eta\tau_Q}, \tag{30}$$

where $\eta = 4\bar{J}_{aa}^2/\Delta U_{aa}$. We evaluate the density of defects \mathcal{D} using equation (24) with $|\Psi_g(t_i)\rangle = |g(0)\rangle$ and $|\Psi_e(\hat{t})\rangle = |e(\hat{t})\rangle$. In order to simplify the expression of \mathcal{D} , we have set $\theta(0) = \pi/2$, which is a greater value than the one we would obtain using the real parameters of the system. This has no significant physical consequences in our case as it is actually equivalent to considering a smaller energy gap in the small lattice limit. The density of defects is then given by

$$\mathcal{D} = \frac{1}{2}(1 - \sin \hat{\theta}), \tag{31}$$

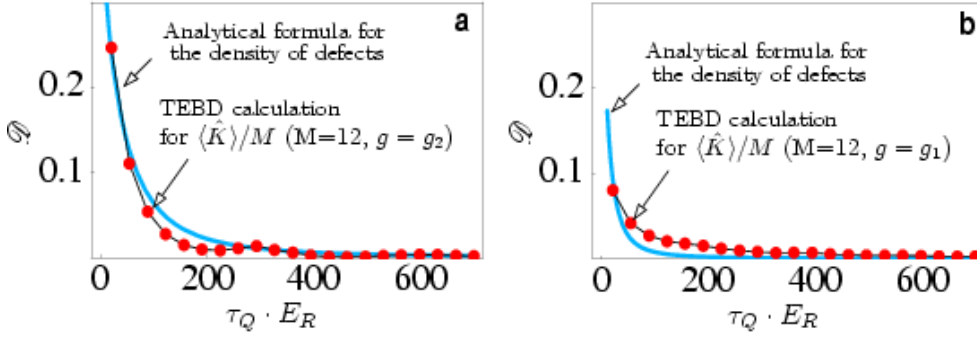


Figure 9. Comparison between the analytical formula for the density of defects (solid line) and the results of the TEBD calculations for the density of kinks $\mathcal{D} = \langle \hat{K} \rangle / M$, for a system of $M = 12$ sites with (a) $g = g_2$ and $\alpha = \sqrt{2}$ and (b) $g = g_1$ and $\alpha = 154$. Using the parameters shown in figure 4, we have $U_{\text{init}}/g_2 = 6.8$, $\Delta U_{aa}/g_2 = 16.4$, $\bar{J}_{aa}/E_R = 0.027$.

where $\hat{\theta} = \theta(\hat{t})$. Inverting equation (31), we obtain

$$\tau_Q(\mathcal{D}) = \frac{1}{\alpha} \frac{\Delta U_{aa}}{16 \bar{J}_{aa}^2} \frac{(1 - 2\mathcal{D})^2}{\sqrt{\mathcal{D}(1 - \mathcal{D})}}, \quad (32)$$

which gives an approximate analytical expression of the quench time τ_Q required to obtain a density of defects \mathcal{D} .

In our system, defects correspond mainly to doubly occupied sites. Thus, the number of defects is approximately measured by the operator

$$\hat{K} = \sum_{i=1}^M \hat{n}_i^a (\hat{n}_i^a - 1). \quad (33)$$

Hence, the density of defects is given by $\mathcal{D} = \langle \hat{K} \rangle / M = \langle (\hat{n}_i^a)^2 \rangle - \langle \hat{n}_i^a \rangle$. Numerical calculations show that the density of defects \mathcal{D} has the same scaling behaviour as $\Delta n_{a,i}^2$. A comparison between equation (31) and the numerical values of the density of defects in the large lattice limit for different values of the ramping time τ_Q is shown in figure 9. For $M = 12$ particles and $g = g_2$, we find that the analytical formula for \mathcal{D} fits the numerical data well for $\alpha = 1.41$. For $g = g_1$ the fit is less accurate. This is expected since for this value of g , the system has a less distinct separation between the adiabatic and impulse regime than for $g = g_2$. For the number of particles we have been able to simulate, the fit improves as we increase the number of particles for both values of g . In addition to this, we see from equation (32) that the time required to initialize a register with a given fidelity—and thus the adiabatic time for small \mathcal{D} —scales with the ratio $\Delta U_{aa}/\bar{J}_{aa}^2$.

4. Conclusion

We have shown that the dynamics of an optical lattice whose periodicity is doubled via superlattice potentials is very well described by a two-mode Hubbard-like Hamiltonian. The parameters of this Hamiltonian have been evaluated in the tight binding approximation using optimally localized GWFs. The doubling of the period removes

half of the lattice sites and doubles the filling factor. We have shown that this doubling can be used for the fast initialization of a quantum register. By starting from a half filled lattice in the small lattice limit filled by either a TG ($g = g_1$) gas or a superfluid ($g = g_2$), a commensurate MI state corresponding to an atomic quantum register can be obtained on timescales shorter than those achieved by direct quantum freezing of a superfluid with same lattice spacing. Furthermore, we derived an analytical expression for the density of defects as a function of the quench time for linear ramping of the superlattice. We found that the time required to achieve a given density of defects is proportional to the ratio $\Delta U_{aa}/\bar{J}_{aa}^2$.

Our numerical calculations of ground state properties suggest that doubling the lattice period drives the system through a quantum phase transition for large lattices $M \rightarrow \infty$. The eventual abrupt change in the ground state properties might be observable by time-of-flight measurements. An investigation of whether such a quantum phase transition indeed exists is beyond the scope of the current work but will be investigated in future work.

In this work we concentrated on the transition from filling factor $n = 1/2$ to $n = 1$. We finally note that the idea developed in this paper may be extended by considering lattices with an initial filling factor of $n = 1/2^\ell$ (where ℓ is an integer). Subsequently removing every second barrier will create a lattice with period $2a$ and filling factor $1/2^{\ell-1}$. This procedure could be repeated ℓ times providing a lattice with filling factor $n = 1$ and large lattice spacing $2^\ell a$.

5. Acknowledgments

This work was supported by the EU through the STREP project OLAQUI and a Marie Curie Intra-European Fellowship within the 6th European Community Framework Programme. The research was also supported by the EPSRC (UK) through the QIP IRC (GR/S82716/01) and project EP/C51933/01. DJ thanks the Beijing International Center for Mathematical Research at Peking University for hospitality while carrying out parts of this work.

Appendix

Appendix A. Definition and localization properties of GWFs

In the TB limit, the effective single particle Hamiltonian of our system in momentum space (in the basis $|\alpha\rangle_q = [(1/\sqrt{M}) \sum_{i=1}^M e^{iqai} \hat{\alpha}_i^\dagger] |0\rangle$ with $\alpha = a, b$) can be written as

$$\hat{H}_{0,q} = \sum_{\mu=0,1} \hat{\varepsilon}(\mu) e^{-ia\mu q}. \quad (\text{A.1})$$

The elements of the matrices $\hat{\varepsilon}(\mu)$ are given by [43]

$$\varepsilon_{\alpha\beta}(\mu) = \langle w_{\alpha,i} | \hat{h}_{0,x} | w_{\beta,i+\mu} \rangle. \quad (\text{A.2})$$

For $\mu = 0$ and $\mu = 1$, the elements of the matrices $\hat{\varepsilon}(\mu)$ correspond to the local site energy and hopping matrix elements between neighbouring sites, respectively. For the TB approximation to be accurate, we need the eigenvalues $E_{\alpha,q}$ of $\hat{H}_{0,q}$ to reproduce very closely the band structure of the exact single particle Hamiltonian $\hat{h}_{0,x}$ for all values of the lattice profile s . If we were to use WFs as mode functions $w_{\alpha,i}$, the matrices $\hat{\varepsilon}$ would be diagonal [24] and the dispersion relations of the two Bloch bands

sinusoidal. In order to obtain a more accurate description, we use GWFs as mode functions. The definition of GWFs is given by

$$w_{\alpha,i}(x,s) = \sqrt{\frac{a}{2\pi}} \int_{-\frac{\pi}{a}}^{\frac{\pi}{a}} dq e^{-iqR_i} \tilde{\Psi}_{\alpha,q}(x,s), \quad (\text{A.3})$$

where $\tilde{\Psi}_{\alpha,q} = \sum_{\beta=a,b} U_{\beta,\alpha}^{(q)*} \Psi_{\beta,q}$ is called the *generalized-Bloch orbital* with $\Psi_{\alpha,q}$ the Bloch function associated with the band α and R_i is the center of site i [44, 25]. The rows of the 2×2 matrix $U^{(q)}$ contain the (real) normalized eigenvectors of $\hat{H}_{0,q}$ associated with the eigenvalues $E_{\alpha,q}$, that is $\sum_{\mu=a,b} (\hat{H}_{0,q})_{n,\mu} U_{\alpha,\mu}^{(q)} = E_{\alpha,q} U_{\alpha,n}^{(q)}$ [43]. Inserting GWFs in equation (A.2), we recover the elements $\varepsilon_{\alpha\beta}(\mu)$ and, hence, GWFs correspond to the mode functions associated with the effective Hamiltonian $\hat{H}_{0,q}$ [43]. Notice that the definition of GWFs reduces to that of WFs for $U^{(q)} = \mathbb{1}$.

Localization properties of GWFs

Given a valid set of GWFs, another equally valid set of GWFs can be obtained by applying the following transformation on the $U^{(q)}$ matrices

$$U^{(q)} \rightarrow \begin{pmatrix} e^{i\phi_a(q)} & 0 \\ 0 & e^{i\phi_b(q)} \end{pmatrix} U^{(q)}, \quad (\text{A.4})$$

where $\phi_\alpha(q)$ are (real) functions of q which can be chosen freely as long as they do not introduce discontinuities in the generalized Bloch function [45]. The gauge transformation (A.4) is equivalent to re-phasing each Bloch function as $\Psi_{\alpha,q} \rightarrow e^{i\phi_\alpha(q)} \Psi_{\alpha,q}$. Notice that gauge transformations do not affect the value of the parameters V_α and $J_{\alpha,\beta}$ calculated using the relations (7) and (6), respectively, but they alter the localization properties—the spread—of the GWFs. Following the convention suggested by Blount [45], we set the phase functions $\phi_\alpha(q)$ in a manner that leads to maximally localized GWFs. That is, we choose the phase functions such that the resulting GWFs minimize the spread functional

$$\Omega = \sum_{\alpha} \langle x^2 \rangle_{\alpha} - \langle x \rangle_{\alpha}^2, \quad (\text{A.5})$$

where in our case $\alpha = a, b$ while $\langle x^2 \rangle_{\alpha} = \langle w_{\alpha,i} | x^2 | w_{\alpha,i} \rangle$ and $\langle x \rangle_{\alpha} = \langle w_{\alpha,i} | x | w_{\alpha,i} \rangle$ correspond to the center of a GWF and its second moment, respectively.

Expanding $\tilde{u}_{\alpha,q}(x,s) = e^{-iqx} \tilde{\Psi}_{\alpha,q}(x,s)$ into plane waves yields

$$\tilde{u}_{\alpha,q}(x,s) = \sum_j G_{\alpha,j}(q,s) e^{iK_j x}, \quad (\text{A.6})$$

where $K_j = 2\pi j/L$ with $L = Ma$. Invoking the translational symmetry of the lattice and the convolution theorem [45], the value of the functional Ω is minimized when the expansion coefficients $G_{\alpha,j}(q,s)$ are chosen real, which is always possible when the lattice possesses mirror symmetry [43]. This is equivalent to the choice of purely real GWFs for even generalized-Bloch functions and purely imaginary ones for odd generalized-Bloch functions. Notice that this conclusion is in agreement with a conjecture of Marzari *et al.* [25] on the real nature (up to a global phase) of maximally localized WFs.

We have numerically evaluated the phases $\phi_\alpha(q)$ using the algorithm described in [25] for the special case of 1D WFs. This procedure minimized the functional Ω in the limit of very fine sampling of the q -space. The effect of this localization procedure is illustrated in figure 3a.

Appendix B. Parameters of the single-particle Hamiltonian

We diagonalize \hat{H}_0 in momentum space for periodic boundary conditions. Using the Fourier transformations $\hat{a}_i = (1/\sqrt{M}) \sum_q e^{iqai} \hat{a}_q$ and $\hat{b}_i = (1/\sqrt{M}) \sum_q e^{iqai} \hat{b}_q$, \hat{H}_0 becomes block diagonal

$$\hat{H}_0 = \sum_q \hat{H}_{0,q}, \quad (\text{B.1})$$

where $q = 2\pi\nu/Ma$, $\nu = 1 \dots M$. In the basis $\{|a\rangle_q, |b\rangle_q\}$, the operator $\hat{H}_{0,q}$ reads

$$\hat{H}_{0,q} = \begin{pmatrix} V_a - 2J_{aa} \cos qa & -i2J_{ab} \sin qa \\ i2J_{ab} \sin qa & V_b + 2J_{bb} \cos qa \end{pmatrix}, \quad (\text{B.2})$$

with $|a\rangle_q = \hat{a}_q^\dagger|0\rangle$ and $|b\rangle_q = \hat{b}_q^\dagger|0\rangle$. For simplicity, the explicit dependence of the parameters on the lattice profile has been dropped.

Due to the periodicity of the lattice, the eigenvalues of $\hat{H}_{0,q}$ exhibit a band structure. By choosing the points $q = 0, \pi/a, \pi/2a$ in the Brillouin zone, we derive and solve a set of equations for the parameters V_α and $J_{\alpha,\beta}$ as functions of the eigenvalues $E_{\alpha,q}$ of $\hat{H}_{0,q}$

$$\begin{aligned} J_{aa} &= \frac{E_{a,\pi} - E_{a,0}}{4}, & J_{bb} &= \frac{E_{b,0} - E_{b,\pi}}{4}, \\ V_a &= \frac{E_{a,0} - E_{a,\pi}}{2}, & V_b &= \frac{E_{b,0} - E_{b,\pi}}{2}, \\ J_{ab} &= \frac{1}{4} [(E_{b,\frac{\pi}{2}} - E_{a,\frac{\pi}{2}})^2 - (V_a - V_b)^2]^{\frac{1}{2}}. \end{aligned} \quad (\text{B.3})$$

For the eigenvalues of $\hat{H}_{0,q}$ to reproduce the band structure of the exact single-particle Hamiltonian along the x -direction $\hat{h}_{0,x}$, we evaluate the parameters V_α and $J_{\alpha,\beta}$ using the eigenvalues $\varepsilon_{\alpha,q}$ of $\hat{h}_{0,x}$ obtained via exact numerical diagonalization for the same points in the Brillouin zone (see figure 2). The numerical values of the parameters obtained via this procedure are shown in figure 4a.

The accuracy of the TB approximation can be tested by evaluating the standard deviation between the exact and approximated band structure. That is, taking N_q different points q_i on each band, we define the standard deviation between the exact and approximate band structure for a given lattice profile by $\sigma_s^2 = (1/2N_q) \sum_{i=1}^{N_q} (\Delta\varepsilon_{a,q_i}^2 + \Delta\varepsilon_{b,q_i}^2)$, with $\Delta\varepsilon_{\alpha,q_i} = \varepsilon_{\alpha,q_i} - E_{\alpha,q_i}$. Averaging over N_s different lattice profiles s_i , we obtain $\langle\sigma\rangle_s = [(1/N_s) \sum_{i=1}^{N_s} \sigma_{s_i}^2]^{\frac{1}{2}} = 3.4 \times 10^{-2} E_R$ for a lattice depth of $V_0 = 10 E_R$. This excellent agreement improves further as we increase the value of V_0 , and hence fully justifies the tight-binding approximation.

Appendix C. Dynamical and ground state calculations using the TEBD algorithm

The TEBD algorithm is based on directly manipulating a matrix product representation of the many-body wave function. Here, we shall briefly describe the key aspects of this algorithm and refer the reader to some of the recent literature [46, 47, 48, 49] for more detail.

An arbitrary state of a 1D quantum lattice system composed of M sites can be written as

$$|\psi\rangle = \sum_{j_1=1}^{\mathfrak{d}} \cdots \sum_{j_M=1}^{\mathfrak{d}} c_{j_1 \cdots j_M} |j_1, \dots, j_M\rangle, \quad (\text{C.1})$$

where $c_{j_1 \cdots j_M}$ is a set of \mathfrak{d}^M complex amplitudes and $|j_m\rangle$ is a basis spanning the local \mathfrak{d} -dimensional Hilbert space of site m . Within time-dependent DMRG the amplitudes $c_{j_1 \cdots j_M}$ are constructed from a product of tensors

$$c_{j_1 j_2 \cdots j_M} = \sum_{\{\alpha\}=1}^{\{\chi\}} \Gamma_{\alpha_1}^{[1]j_1} \lambda_{\alpha_1}^{[1]} \Gamma_{\alpha_1 \alpha_2}^{[2]j_2} \lambda_{\alpha_2}^{[2]} \cdots \Gamma_{\alpha_{M-1}}^{[M]j_M}, \quad (\text{C.2})$$

where $\{\alpha\} = \{\alpha_1, \dots, \alpha_{M-1}\}$, $\{\chi\} = \{\chi_1, \dots, \chi_{M-1}\}$ and with Γ and λ tensors chosen to be constructed from the set of $M-1$ Schmidt decompositions for contiguous partitions of the system. Specifically, the elements of $\lambda_{\alpha}^{[m]}$ are taken to be Schmidt coefficients of the bipartite splitting after site m in $|\psi\rangle = \sum_{\alpha=1}^{\chi_m} \lambda_{\alpha}^{[m]} |L_{\alpha}^m\rangle |R_{\alpha}^m\rangle$ with Schmidt rank χ_m . The Schmidt states $|L_{\alpha}^m\rangle$ and $|R_{\alpha}^m\rangle$ spanning the left $\{1, \dots, m\}$ and right $\{m+1, \dots, M\}$ subsystems of sites respectively are then specified by the corresponding sums remaining in equation (C.2).

The usefulness of this representation is based on the observation that for 1D systems with a Hamiltonian composed of nearest neighbour terms the groundstate and low-lying excited states have Schmidt coefficients $\lambda_{\alpha}^{[m]}$ which rapidly decay with α when arranged in descending order. Consequently, rather than allowing the Schmidt ranks χ_m to grow to their maximum permissible value a much smaller fixed upper-limit χ can be imposed truncating the representation while still providing a near unit overlap with the exact state $|\psi\rangle$. Fixing the Schmidt ranks results in the number of parameters scaling as $O(\mathfrak{d}\chi^2 M)$ and so curtails the possible exponential growth with M seen for general coefficients $c_{j_1 \cdots j_M}$.

The matrix product representation also permits the efficient update of the state after the action of a unitary operator on any two neighboring lattice sites. This proceeds by modifying the Γ tensors associated to the sites and the λ tensor linking them and requiring a number of operations which scales as $O(\mathfrak{d}^4 \chi^3)$. The resulting tensors are then systematically truncated back to a maximum rank of χ .

Dynamical simulations can be performed by decomposing the time evolution operator $\exp(-iH\delta t)$, for small time step δt , into a sequence of pairwise unitaries via a Suzuki-Trotter expansion. Given the properties outlined such a calculation is likely to be accurate for a practical value of χ if both the initial state and the states generated by the dynamics remain in the low-energy manifold of the system. To determine the appropriate χ calculations are repeated with increasing values of χ until the final result converges and are unaffected by further increases. For practical purposes the convergence is usually quantified by the robustness of the expectation values calculated. The accuracy of a calculation is also gauged by the sum of the discarded Schmidt coefficients at each time step - a quantity which should necessarily be small - and the deviation of normalization of the final state from unity which indicates the accumulated effect of truncation.

Finally, initial states are typically taken to be the groundstate of the system which are found either by applying the DMRG procedure or, as in this work, by simulating imaginary time evolution through the repeated application of $\exp(-H\delta t)$ and subsequent renormalization of the state. In our simulations, we have used $\chi = 40$.

Appendix D. The ramp s_{gap}

The ramp s_{gap} can be evaluated as follows. The energy gap between the ground and the first excited state associated with a given lattice profile s is given by $\text{gap}(s) = \omega_{0e}$ where $\omega_{0k} = (\varepsilon_{\text{eff},k} - \varepsilon_{\text{eff},0})$ with $\varepsilon_{\text{eff},\alpha}$ the α -th instantaneous eigenvalue of $\hat{H}_{\text{eff}}(s)$. The gap is evaluated numerically via the direct diagonalization of \hat{H}_{eff} for a small number of sites. The function $s_{\text{gap}}(t)$ is defined by the equation $ds_{\text{gap}}(t)/dt = \text{gap}(s_{\text{gap}}(t))/K$ where $K^{-1} = \int_0^{\tau_Q} dt \text{gap}(s_{\text{gap}}(t))$ is a normalization constant.

References

- [1] D. Jaksch and P. Zoller. The cold atom hubbard toolbox. *Annals of Physics*, 315:52, 2005.
- [2] Maciej Lewenstein, Anna Sanpera, Veronica Ahufinger, Bogdan Damski, Aditi Sen De, and Ujjwal Sen. Ultracold atomic gases in optical lattices: Mimicking condensed matter physics and beyond. (*Preprint cond-mat/0606771*), 2006.
- [3] J. I. Cirac and P. Zoller. New frontiers in quantum information with atoms and ions. *Physics Today*, 57(3):38, March 2004.
- [4] D. Jaksch, H.-J. Briegel, J. I. Cirac, C. W. Gardiner, and P. Zoller. Entanglement of atoms via cold controlled collisions. *Phys. Rev. Lett.*, 82:1975, 1999.
- [5] Olaf Mandel, Markus Greiner, Artur Widera, Tim Rom, Theodor W. Hänsch, and Immanuel Bloch. Coherent transport of neutral atoms in spin-dependent optical lattice potentials. *Phys. Rev. Lett.*, 91:010407, 2003.
- [6] R. Raussendorf and H.-J. Briegel. A one-way quantum computer. *Phys. Rev. Lett.*, 86:5188, 2001.
- [7] K. G. H. Vollbrecht, E. Solano, and J. I. Cirac. Ensemble quantum computation with atoms in periodic potentials. *Phys. Rev. Lett.*, 93(22):220502–4, November 2004.
- [8] Zheng-Wei Zhou, Yong-Jian Han, and Guang-Can Guo. Local operations in qubit arrays via global periodic manipulation. *Phys. Rev. A*, 74(5):052334–5, November 2006.
- [9] Alastair Kay and Jiannis K. Pachos. Quantum computation in optical lattices via global laser addressing. *New J. Phys.*, 6:126–126, 2004.
- [10] T. Calarco, U. Dorner, P. S. Julienne, C. J. Williams, and Peter Zoller. Quantum computations with atoms in optical lattices: Marker qubits and molecular interactions. *Phys. Rev. A*, 70:012306, 2004.
- [11] For example, in ion trap quantum computing, distances in the μm regime are sufficient to address individual atoms. See, e.g. H. Häffner, W. Hänsel, C. F. Roos, J. Benhelm, D. Chek-al-kar, M. Chwalla, T. Körber, U. D. Rapol, M. Riebe, P. O. Schmidt, C. Becher, O. Gühne, W. Dür, and R. Blatt, *Nature* **438**, 643 (2005).
- [12] M. Greiner, O. Mandel, T. Esslinger, T. W. Hänsch, and I. Bloch. Quantum phase transition from a superfluid to a mott insulator in a gas of ultracold atoms. *Nature*, 415:39, 2002.
- [13] P. S. Julienne, C. J. Williams, Y. B. Band, and Marek Trippenbach. Loading bose-einstein-condensed atoms into the ground state of an optical lattice. *Phys. Rev. A*, 72(5):053615–7, November 2005.
- [14] Shlomo E. Sklarz, Inbal Friedler, David J. Tannor, Yehuda B. Band, and Carl J. Williams. Flat-phase loading of a bose-einstein condensate into an optical lattice. *Phys. Rev. A*, 66(5):053620–, November 2002.
- [15] S. R. Clark and Dieter Jaksch. Dynamics of the superfluid to mott-insulator transition in one dimension. *Phys. Rev. A*, 70:43612, 2004.
- [16] P. B. Blakie and J. V. Porto. Adiabatic loading into optical lattices. *Phys. Rev. A*, 69:013603, 2004.
- [17] Ana Maria Rey. *Ultra-cold bosonic atoms in optical lattices*. PhD thesis, Univ. of Maryland at College Park, 2004.
- [18] S. Peil, J. V. Porto, B. Laburthe Tolra, J. M. Obrecht, B. E. King, M. Subbotin, S. L. Rolston, and W. D. Phillips. Patterned loading of a bose-einstein condensate into an optical lattice. *Phys. Rev. A*, 67(5):051603–, May 2003.
- [19] J. Sebby-Strabley, M. Anderlini, P. S. Jessen, and J. V. Porto. Lattice of double wells for manipulating pairs of cold atoms. *Phys. Rev. A*, 73:033605, 2006.
- [20] Olivier Gygi, Helmut G. Katzgraber, Matthias Troyer, Stefan Wessel, and G. George Batrouni. Simulations of ultracold bosonic atoms in optical lattices with anharmonic traps. *Physical Review A (Atomic, Molecular, and Optical Physics)*, 73(6):063606, 2006.

- [21] T. P. Meyrath, F. Schreck, J. L. Hanssen, C.-S. Chuu, and M. G. Raizen. Bose-einstein condensate in a box. *Physical Review A (Atomic, Molecular, and Optical Physics)*, 71(4):041604, 2005.
- [22] Dieter Jaksch, C. Bruder, J.I. Cirac, C.W. Gardiner, and P. Zoller. Cold bosonic atoms in optical lattices. *Phys. Rev. Lett.*, 81:3108, 1998.
- [23] N. W. Ashcroft and N. D. Mermin. *Solid State Physics*. Brooks/Cole Thomson Learning, Philadelphia, 1976.
- [24] I. Schnell, G. Czycholl, and R. C. Albers. Hubbard-u calculations for cu from first-principle wannier functions. *Phys. Rev. B*, 65:075103, 2002.
- [25] Nicola Marzari and David Vanderbilt. Maximally localised generalised wannier functions for composite energy bands. *Phys. Rev. B*, 56(20):12847, November 1997.
- [26] Till D. Kühner, Steven R. White, and H. Monien. One-dimensional bose-hubbard model with nearest-neighbor interaction. *Phys. Rev. B*, 61:12474, 2000.
- [27] Robert Roth and Keith Burnett. Phase diagram of bosonic atoms in two-color superlattices. *Phys. Rev. A*, 68:023604, 2003.
- [28] Belen Paredes, Artur Widera, Valentin Murg, Olaf Mandel, Simon Folling, Ignacio Cirac, Gora V. Shlyapnikov, Theodor W. Hansch, and Immanuel Bloch. Tonks-girardeau gas of ultracold atoms in an optical lattice. *Nature*, 429(6989):277–281, May 2004.
- [29] L. I. Schiff. *Quantum Mechanics*. Mc-Graw-Hill, 3rd edition, 1968.
- [30] S. R. Clark and D. Jaksch. Signature of the superfluid to mi-insulator transition in the excitation spectrum of cold atoms. *New J. Phys.*, 8:160, 2006.
- [31] J. Hecker Denschlag, J. E. Simsarian, H. Haefner, C. McKenzie, A. Browaeys, D. Cho, K. Helmerson, S. L. Rolston, and W. D. Phillips. A bose-einstein condensate in an optical lattice. *J. Phys. B: At. Mol. Opt. Phys.*, 35:3095–3110, 2002.
- [32] A. Griessner, A. J. Daley, S. R. Clark, D. Jaksch, and P. Zoller. Dissipative dynamics of atomic hubbard models coupled to a phonon bath: Dark state cooling of atoms within a bloch band of optical lattices. (*Preprint cond-mat/0612263*), 2006.
- [33] Thorsten Kohler, Krzysztof Goral, and Paul S. Julienne. Production of cold molecules via magnetically tunable feshbach resonances. *Reviews of Modern Physics*, 78(4):1311, 2006.
- [34] Tino Weber, Jens Herbig, Michael Mark, Hanns-Christoph Nagerl, and Rudolf Grimm. Bose-einstein condensation of cesium. *Science*, 299(5604):232–235, 2003.
- [35] C. J. Pethick and H. Smith. *Bose-Einstein Condensation in Dilute Gases*. Cambridge University Press, 2002.
- [36] Bogdan Damski. The simplest quantum model supporting the kibble-zurek mechanism of topological defect production: Landau-zener transitions from a new perspective. *Phys. Rev. Lett.*, 95:035701, 2005.
- [37] Bogdan Damski and Wojciech H. Zurek. Adiabatic-impulse approximation for avoided level crossings: from phase transition dynamics to landau-zener evolutions and back again. *Phys. Rev. A*, 73:063405, 2006.
- [38] Fernando M. Cucchiatti, Bogdan Damski, Jacek Dziarmaga, and Wojciech H. Zurek. Dynamics of the bose-hubbard model: transition from mott insulator to superfluid. *Phys. Rev. A*, 75:023603, 2007.
- [39] W. H. Zurek. Cosmological experiments in superfluid helium. *Nature*, 317:505, 1985.
- [40] C. Zener. Non-adiabatic crossing of energy levels. *Proc. Roy. Soc. London Ser. A*, 137:696, 1932.
- [41] Nikolai Sinitsyn. *Generalisation of the Landau-Zener theory in the physics of nanoscale systems*. PhD thesis, Texas A&M University, 2004.
- [42] Jan R. Rubbmark, Michael M. Kash, Michael G. Littman, and Daniel Kleppner. Dynamical effects at avoided level crossings: A study of the landau-zener effect using rydberg atoms. *Phys. Rev. A*, 23:3107, 1981.
- [43] B. Sporkmann and H. Bross. Calculation of wannier functions for fcc transition metals by fourier transformation of bloch functions. *Phys. Rev. B*, 49:10869, 1994.
- [44] Helmut Bross. A general interpolation scheme for the one-electron energies of a solid. *Z. Physik*, 243:311–325, 1971.
- [45] E. I. Blount. *Solid state physics: advances in research and applications*, chapter Formalisms of Band Theory, page 305. Academic Press, 1962.
- [46] Guifré Vidal. Efficient classical simulation of slightly entangled quantum computations. *Phys. Rev. Lett.*, 91:147902, October 2003.
- [47] Guifré Vidal. Efficient simulation of one-dimensional quantum many-body systems. *Phys. Rev. Lett.*, 93:40502, July 2004.
- [48] G. Vidal. Classical simulation of infinite-size quantum lattice systems in one spatial dimension.

(Preprint *cond-mat/0605597*), 2006.

- [49] A. J. Daley, C. Kollath, U. Schollwöck, and G. Vidal. Time-dependent density-matrix renormalization-group using adaptive effective hilbert spaces. *Journal of Statistical Mechanics: Theory and Experiment*, 2004(04):P04005, 2004.